Research Square

Preprints are preliminary reports that have not undergone peer review.
They should not be considered conclusive, used to inform clinical practice,
or referenced by the media as validated information.

# Do AI weather models learn atmospheric perturbation growth characteristics? A FuXi case study based on Breeding of Growing Modes method

**Xiao Shang**
National University of Defense Technology
**Jiping Guan**
guanjiping@nudt.edu.cn
National University of Defense Technology
**Jun Peng**
National University of Defense Technology
**Chunqiao Lin**
National University of Defense Technology
**Lifeng Zhang**
National University of Defense Technology

**Article**

**Keywords:** Breeding of Growing Modes, FuXi, AI weather models, MPAS, perturbation growth, physical consistency

**Posted Date:** November 9th, 2026

**DOI:** https://doi.org/10.21203/rs.3.rs-11389396/v1

**License:** This work is licensed under a Creative Commons Attribution 4.0 International License.
Read Full License

**Additional Declarations:** No competing interests reported.

# Do AI weather models learn atmospheric perturbation growth characteristics? A FuXi case study based on Breeding of Growing Modes method

Xiao Shang[1], Jiping Guan[1*], Jun Peng[1*], Chunqiao Lin[1], Lifeng Zhang[1]

[1] College of Meteorology and Oceanography, National University of Defense Technology, Changsha, China.

*Corresponding authors: Prof. Jiping Guan and Prof. Jun Peng

Email: guanjiping@nudt.edu.cn and pengjun@nudt.edu.cn

## Abstract

To assess whether artificial intelligence (AI) weather models learn atmospheric perturbation growth dynamics, we compare the data-driven FuXi model with the dynamical Model for Prediction Across Scales (MPAS) using the Breeding of Growing Modes (BGM) method. MPAS rapidly captures baroclinic and convective instabilities, with perturbations saturating after approximately three days. In contrast, FuXi exhibits a pronounced "delayed growth" feature, with extremely slow growth during the initial two days. Although the saturated perturbations are broadly consistent with synoptic-scale systems in the mid-to-high latitudes, substantial non-physical noise persists in the low latitudes. Sensitivity experiments reveal that initial amplitude linearly determines saturation magnitude, while morphology governs spatial distribution, lacking the nonlinear coupling of numerical models. Perturbation kinetic energy spectra exhibit a "flat-tail" at high wavenumbers, indicating absent energy cascade and weak dissipation. Rotational/divergent decomposition confirms dominance of synoptic-scale rotational energy, failing to capture divergent motions. These findings suggest FuXi learns only partial statistical relationships from coarse-grained data rather than complete multiscale physical evolution, offering new insights for assessing AI weather model predictability and ensemble forecasting.



**Keywords:** Breeding of Growing Modes; FuXi; AI weather models; MPAS; perturbation growth; physical consistency.

## Introduction

A central problem in atmospheric predictability research is to reveal how initial condition uncertainties grow within chaotic dynamical systems and ultimately limit forecast skill[1]. Lorenz's pioneering work demonstrated that, owing to the chaotic nature of atmospheric motion, even minute initial errors grow rapidly and propagate upscale through nonlinear scale interactions, leading to an intrinsic limit of predictability, the phenomenon vividly termed the "butterfly effect"[2-5].

Building upon this theoretical understanding, ensemble forecasting was introduced to characterize forecast uncertainty[6,7]. Its core idea is to generate a set of possible future atmospheric trajectories by perturbing the initial state in physically meaningful ways. Within this framework, the evolution of initial perturbation techniques has constituted a major thread in the development of ensemble forecasting. From early Monte Carlo random perturbations[8] to the Breeding of Growing Modes (BGM) developed at NCEP[9-11], to the Singular Vector (SV) technique adopted at ECMWF[12-14], as well as the Ensemble Kalman Filter (EnKF)[15,16] and Ensemble Data Assimilation (EDA)[17] developed subsequently, initial perturbation techniques have continually striven to capture the most rapidly growing error modes in the atmosphere, enabling ensemble members to maximally cover the space of possible atmospheric trajectories.

In recent years, artificial intelligence (AI) methods represented by deep learning have brought revolutionary changes to weather forecasting[18-22]. Data-driven models[23-34] such as FourCastNet, Pangu-Weather, GraphCast, AIFS, and FuXi not only possess overwhelming advantages in computational efficiency, but their deterministic forecast skill has also reached or even surpassed that of international mainstream physical models, with very low inference cost, providing unprecedented possibilities for constructing ultra-large-scale ensemble forecasts. However, whether

these models truly learn the intrinsic chaotic dynamics of the atmosphere, and in particular whether they can correctly reproduce the error growth dynamics described by the "butterfly effect", remains an open question of central importance, with existing studies yielding divergent conclusions.

Using CMA-GEPS singular vectors as initial perturbations for Pangu-Weather yields medium-range ensemble forecast performance comparable to that of CMA-GEPS, confirming the sensitivity of AI models to traditional perturbation schemes[35]. Sensitivity analyses based on FourCastNet further reveal that the gradient fields generated by AI models closely resemble those from the adjoint modes of physical models, capturing physically meaningful spatiotemporal correlations[36]. Perturbation dynamics experiments on the FuXi model indicated that when initial errors reach a certain threshold, their 72-hour growth magnitude is consistent with that of physical models; the ensemble perturbation generation scheme developed on this basis significantly improved the forecast skill of tropical cyclone tracks[37]. Inspired by these findings, the Conditional Nonlinear Optimal Perturbation (CNOP) method based on AI weather large models has been successfully applied to typhoon track forecasting[38-41], while AI models for El Niño and Madden–Julian Oscillation (MJO) prediction successfully overcame the "predictability barrier" thanks to CNOP initial perturbations[39,42-44]. A case study on Super Typhoon Khanun further confirmed that, in global AI weather models, tiny initial perturbations over two key regions can trigger transitions between two attractors, leading to pronounced differences in predicted storm positions[45]. These studies implies that AI models can effectively capture the intrinsic connections that govern the evolution of atmospheric systems.

However, another series of studies has revealed a profound crisis of physical consistency—for example, their inability to forecast unprecedented "gray swan" weather extremes[46-48] and to reproduce the statistics at small scales[49]. Selz and Craig

pointed out that Pangu-Weather completely fails to simulate the “butterfly effect” triggered by extremely small-amplitude initial perturbations, instead erroneously suggesting that the atmosphere has infinite predictability[50]. Further studies found that AI models exhibit systematic biases in mesoscale kinetic energy spectra, geostrophic balance, and the ratio of rotational to divergent wind components, indicating insufficient physical fidelity[51]. Selz and Craig subsequently conducted a systematic evaluation of GraphCast, FourCastNet, Aurora, NeuralGCM, GenCast and other models, further indicating that the performance of these AI models can be categorized into two types: one type exhibits no “butterfly effect” characteristics at all; the other type, although showing signs of rapid initial growth, stems from non-physical numerical noise rather than real physical processes, and the results of some models are highly dependent on the running hardware (CPU versus GPU results differ significantly)[52]. Recently, spectral analyses of four probabilistic MLWP models (NeuralGCM-ENS, FourCastNet 3, AIFS-ENS and GenCast) further revealed that their difference kinetic energy (DKE) spectra exhibit anomalously flat "white noise" features at high wavenumbers, failing to reproduce the physical behavior of upscale error propagation in numerical models[53,54].

The above contradictions suggest that, although AI models perform well in deterministic forecasts and certain ensemble forecast skills, their perturbation growth dynamics may differ fundamentally from those of the real atmosphere. Hassanzadeh et al. attributed the above deficiencies and the forecast skill of AI models to the same origin: the spatiotemporal coarse-graining of training data, which filters out small-scale processes to enhance medium-range forecast stability, yet at the cost of compromising the physical representation of atmospheric thermodynamic irreversibility and multiscale chaotic behavior[55].

The Breeding of Growing Modes (BGM) method, one of the commonly used

techniques for generating initial perturbations in ensemble forecasting, extracts the most unstable error growth modes in the system through repeated integration and rescaling[9], providing an ideal framework for diagnosing whether AI models learn physically reasonable perturbation evolution laws. This study applies the BGM method to systematically investigate the perturbation growth dynamics of the FuXi AI weather model, aiming to address three core questions: (1) Can the FuXi model generate rapidly growing perturbations consistent with physical laws through BGM? (2) How physically consistent are the spatial structures of the bred modes? (3) What are the scale dependence and energy evolution characteristics of the breeding process, and how do they differ from traditional numerical models? These findings will offer a new perspective for assessing the predictability of AI weather models and provide a methodological foundation for developing AI ensemble forecasting systems.

## Results

### Perturbation Breeding Process

#### *Perturbation evolution curves*

With $\omega$ set to 1.0, perturbation breeding experiments were conducted. Fig. 1 shows the variations of the perturbation magnitude, growth rate, sign index, and correlation coefficient of geopotential height at 500 hPa, 700 hPa, and 850 hPa with breeding time for FuXi and MPAS. The magnitude of the growing mode is measured by the root-mean-square (RMS) amplitude of the perturbation.

As shown in the right column of Fig. 1, the breeding process of MPAS can be roughly divided into three stages. In the initial stage, perturbations grow rapidly within one day; in particular, within the first 6 hours, the growth rate at 500 hPa geopotential height exceeds 2.5 gpm/6h. This corresponds to a stage of rapid

adjustment in perturbation structure and rapid energy growth, reflecting MPAS's ability to rapidly capture atmospheric instability modes (such as baroclinic instability and convective instability) and effectively filter out "noise" components that are not coordinated with atmospheric dynamical structures. During the subsequent 1–3 days, the perturbation enters a transitional stage during which the growth rate gradually decreases and the RMS growth slows markedly. However, the sign index and correlation coefficient continue to rise steadily, indicating that although the dominant growing structure has been largely established, its spatial configuration and energy distribution are still undergoing "fine-tuning" to better match the fastest-growing perturbation mode of actual analysis errors. After approximately 3 days of breeding cycles, the perturbation reaches saturation in both amplitude and spatial morphology: the amplitude grows to a magnitude comparable to actual analysis errors, and the spatial structure evolves into Local Lyapunov Vectors (LLVs) coordinated with the atmospheric background flow pattern[11,56]. At this point, the saturated perturbation has been established as the "fastest-growing mode", becoming the optimal initial perturbation for ensemble forecasting, effectively representing the error distribution most likely to develop and contribute to forecast uncertainty in the current atmosphere.

The above evolution characteristics are largely consistent with previous findings based on a low-resolution spectral model for global medium-range numerical weather prediction, T63L9[57-59]. Compared with MPAS, FuXi perturbations grow extremely slowly during the first 2 days, with the sign index and correlation coefficient approaching 1.0 (Fig. 1e, g), indicating that the AI model is highly insensitive to the initial noise and lacks the stage of rapid perturbation structure adjustment and energy growth exhibited by MPAS. This may stem from FuXi's data-driven statistical learning paradigm, which lacks the complete physical instability

mechanisms in numerical models that trigger the growth of initial noise. From 2 to 5 days, FuXi perturbations enter the growth stage, with growth rates comparable to the second stage of MPAS. The sign index and correlation coefficient gradually decrease, reflecting that the perturbation is transitioning from the initial simple structure to a complex, realistic error mode. After 5 days, the perturbation tends toward saturation. However, the growth rate exhibits regular "sawtooth" oscillations around 1.0, which is more likely attributable to the model own numerical truncation errors and inherent "statistical equilibrium" characteristics rather than pure dynamical saturation dominated by physical dissipation and nonlinear interactions.

***Spatial structure of perturbations***

The 500 hPa geopotential height perturbation field (shaded) for each breeding cycle and the geopotential height field (contours) from the ERA5 reanalysis at the corresponding time are plotted in Fig. 2. The saturated perturbation fields of FuXi and MPAS are plotted separately as contours in Fig. 3.

Consistent with the evolution of perturbation growth curves, MPAS can rapidly develop continuous perturbation structures with physical consistency at the initial stage of breeding. In the mid-to-high latitudes, perturbations are mainly distributed around trough-ridge systems and high/low pressure centers, reflecting significant baroclinic instability characteristics; in the low latitudes, perturbations are dominated by convective instability structures[60]. The overall spatial morphology is rich and exhibits favorable continuous evolution characteristics as the breeding cycles advance (Fig. 2b).

In contrast, the perturbation evolution of FuXi is markedly delayed: within 1-2 days after breeding, the perturbation field is still dominated by noise, and only around day 2.5 does it gradually develop a spatial distribution consistent with the background synoptic field. Perturbations then begin to grow significantly and

approach saturation around day 5, a characteristic consistent with the perturbation evolution curves (Fig. 1, Fig. 2a). Careful observation of Fig. 2a reveals that the breeding process of FuXi is not a continuous physical evolution, but rather resembles a discrete numerical construction on an effective dynamical system defined by coarse-grained training data. Perturbations accumulate persistently at specific grid points and accelerate the breeding once they acquire a certain spatial structure. The saturated perturbations exhibit a degree of physical consistency at large scales, predominantly concentrating near strong synoptic systems such as large troughs and ridges, high- and low-pressure centers in the mid-to-high latitudes, but their response to weak synoptic systems is limited, with substantial residual noise in the low latitudes (Fig. 3a). This behavior primarily arises because purely data-driven AI models still learn only partial statistical features of atmospheric dynamics from coarse-grained data, rather than the complete multiscale physical evolution. Random noise is more akin to an "outlier" for the model and is readily suppressed by statistical inertia. As a result, the model cannot adequately respond to perturbations at small-to-mesoscale.

## Initial Perturbation Sensitivity

Previous studies have shown that the magnitude of the initial perturbation directly affects the efficiency and results of the breeding cycle in numerical models, owing to the nonlinear physical processes involved[57]. Perturbation dynamics experiments on the FuXi model further indicated that the initial perturbation must reach a certain amplitude and possess a certain physical structure to grow significantly in the model[37]. Accordingly, this section examines the influence of the magnitude and structure of the initial perturbation on the FuXi breeding process, respectively.

### *Influence of initial perturbation magnitude*

Sensitivity experiments were conducted with $\omega$ = 0.2, 0.4, 0.5, 0.6, 0.8, and 1.0. The results are shown in Fig. 4. Under different $\omega$ values, the breeding curve trends of FuXi are essentially consistent. Taking 500 hPa geopotential height as an example, the RMS magnitude of the perturbation field is mainly determined by the initial perturbation amplitude, with the two being approximately linearly related. The growth rate curves nearly coincide for different ω values, indicating that FuXi does not exhibit the typical initial-value nonlinear sensitivity characteristic of traditional numerical models. The correlation coefficient varies little with $\omega$, but the sign index decreases as $\omega$ decreases. Analyzing the spatial fields of the saturated perturbations (not shown), the distribution of sensitive regions is almost completely consistent with Fig. 2a and Fig. 3a, indicating that the dominant modes of the saturated perturbations are not sensitive to the initial magnitude. Nevertheless, the smaller $\omega$, the denser the noise in the perturbation field, particularly at low latitudes, indicating that small-amplitude perturbation noise oscillates in isolation around zero values and is difficult to filter out effectively.

***Influence of initial perturbation morphology***

Perlin noise was used to replace the original random number field uniformly distributed on [-1,1], in order to further explore the influence of initial perturbation morphology on the FuXi breeding process. Multiple sets of parameter experiments were designed as listed in Table. 1. The RMS and sign index evolution curves are shown in Fig. 5. The growth rate and correlation coefficient curves exhibit similar variation patterns and are therefore not repeated here. The spatial distributions of the saturated perturbations are shown in Fig. 6.

Comparing the breeding curves of the random number field (Fig. 1) and the Perlin noise field (Fig. 5), the Perlin-noise-driven experiments exhibit sustained RMS growth from the very beginning of breeding, skipping the “smoothing period”

of the first 2 days observed with the random number field. This is mainly attributed to the inherently good spatial continuity of Perlin noise. Further comparison of the Group 1 experiments reveals that the smaller the Scale value, the larger the spatial scale of the perturbation and the faster the breeding speed; when Scale is set to 2, it even exhibits characteristics of high initial growth rate similar to MPAS. However, the influence of Scale on the breeding result is not a simple linear relationship; rather, there exists a certain threshold beyond which its modulating effect on the breeding process tends to saturate. This threshold may be closely related to the model's own effective resolution. The Group 2 experimental results show that the smaller the Octaves value, the fewer detail levels the initial perturbation contains, but the larger the perturbation amplitude, which in turn leads to a correspondingly larger output perturbation amplitude at saturation. The Group 3 experiments on Persistence exhibit similar trends. Furthermore, the trend of the evolution curves for these two groups of experiments is largely independent of their respective parameters, with only the magnitudes differing.

From the spatial fields of the saturated perturbations, the three experiments of Group 1 are noticeably different (Fig. 6a, b). Compared with white noise (Fig. 2), the mid-latitude structure is more abundant, but the process and result are still discontinuous, with substantial noise generally present in the low latitudes. The distributions of the saturated perturbations for Group 2 and Group 3 are almost completely consistent, as shown in the red and blue boxes in Fig. 6b, c, and d. This indicates that the breeding result mainly depends on the spatial distribution of the initial perturbation and is independent of the specific details. Moreover, even if the initial field possesses good spatial continuity, its evolution remains difficult to maintain, further supporting that the FuXi breeding process is not a natural evolution based on physical mechanisms, but is closer to a numerical sense of error

accumulation process.

## Perturbation Kinetic Energy Spectrum

### *Total perturbation kinetic energy*

To evaluate the evolution characteristics of perturbation energy during the breeding cycle in the AI model, this section analyzes the perturbation kinetic energy (PKE) spectrum during the cycle (Fig. 7). In the MPAS breeding process, small-scale (wavelength $l < 150km$) energy dissipates rapidly. This is consistent with Skamarock et al.'s finding that the effective resolution of MPAS is approximately 6 times the grid spacing[61], while large-scale PKE grows rapidly and the spectral peak continues to shift toward lower wavenumbers, indicating that the unstable modes captured by MPAS continue to develop. FuXi exhibits evolution trends similar to MPAS at large scales but differs significantly at small and medium scales, particularly in the high-wavenumber region, where a marked "flat-tail" characteristic is observed. When the initial perturbation is white noise, the spectrum even "turns up," with energy decaying extremely slowly, indicating that FuXi lacks an effective physical dissipation mechanism, manifested as substantial noise in physical space. Furthermore, the effective resolution of FuXi may be markedly lower than that of MPAS[62], allowing it to capture only perturbation modes with $l > 200km$.

Compared with random noise, the Perlin-noise-driven breeding process has a faster energy response: the small-scale spectral region enters the "flat-tail" state earlier, and the initial perturbation energy spectrum curve of Exp 9 approaches the saturated shape at the very beginning of breeding, indicating that perturbations with good spatial coherence and multi-scale structure can accelerate the breeding process.

### *Rotational kinetic energy and divergent kinetic energy*

The PKE spectrum can be further decomposed into rotational and divergent

components via the Helmholtz theorem[63,64]. Rotational kinetic energy represents the kinetic energy contributed by the rotational wind component, reflecting the intensity and evolution of synoptic-scale systems such as cyclones and anticyclones. Divergent kinetic energy represents the kinetic energy contributed by the divergent wind component, primarily indicating the activity of processes related to vertical motion. Their relative magnitudes at different wavenumbers provide important physical evidence for diagnosing energy changes during the breeding process[65,66].

As shown in Fig. 8b, MPAS exhibits comparable rotational and divergent kinetic energy at all scales, indicating that both baroclinic instability and convective instability are fully developed, ultimately forming saturated perturbations encompassing unstable modes across all scales. In contrast, FuXi shows distinctly different characteristics: regardless of the initial field, the divergent kinetic energy captured by FuXi in convective instability is markedly weaker, and the saturated perturbations are dominated by rotational kinetic energy of synoptic-scale systems (Fig. 8a, c, d), distributed around large troughs and ridges and high/low pressure system centers in the mid-to-high latitudes (Figs. 2 and 6). For random noise, both rotational and divergent kinetic energy decay slowly at scales of $l < 200km$, particularly at smaller scales ($l < 100km$), where their proportions change extremely little, always maintaining at approximately 50%. This corresponds to the widespread noise in the perturbation field in the low latitudes and is mainly attributed to the lack of physical-model dissipation in FuXi.

## Discussion

This study systematically compared the perturbation growth dynamics of the data-driven model FuXi and the traditional dynamical model MPAS using the Breeding of Growing Modes (BGM) method. The results reveal fundamental

differences between the two models in terms of perturbation evolution paths, saturation characteristics, and energy evolution, with important implications for the predictability assessment and ensemble forecasting applications of AI weather models.

First, FuXi exhibits a significant "delayed growth" characteristic in the breeding cycle: perturbations hardly grow during the initial stage of breeding (approximately the first 2 days), and require smoothing of random noise before entering the rapid growth stage and ultimately reaching saturation. The evolution curves with Perlin noise confirm this process. This behavior contrasts sharply with the evolution of MPAS, which rapidly responds to initial noise within one day and quickly captures convective instability and baroclinic instability. These results are consistent with Selz and Craig's evaluation of other AI models, such as Pangu-Weather and GraphCast, further supporting the view that "current mainstream AI models suffer from physical deficiency in simulating the butterfly effect"[50,52].

Second, from the perspective of perturbation morphology evolution, the sign index and correlation coefficient of MPAS gradually rise from low values to saturation, reflecting the successful transformation from initial random noise to perturbation fields with physical structure. In contrast, these two indicators of FuXi are close to 1.0 in the initial stage, indicating that the initial perturbation is highly similar to the noise field and gradually decreases in subsequent breeding. This shows that FuXi's breeding process does not extract unstable modes through physical evolution, but instead tends to "smooth" and "accumulate" the initial perturbation at the numerical level. Although its spatial structure is broadly consistent with the distribution of mid-to-high latitude synoptic systems, it is still composed of isolated values and retains substantial residual noise in the low latitudes. This phenomenon persists even with spatially continuous initial Perlin noise, indicating that what FuXi

has learned is primarily partial statistical characteristics of atmospheric dynamics in coarse-grained data, rather than the full multiscale physical evolution.

In addition, sensitivity experiments on initial perturbation amplitude and morphology show that FuXi's responses to these two factors are essentially independent, lacking the complex nonlinear coupling characteristic of numerical models. Specifically, the initial amplitude linearly determines the magnitude of the saturated perturbation, while the initial morphology mainly governs the spatial distribution of the saturated perturbation.

The perturbation kinetic energy (PKE) spectrum analysis provides quantitative evidence for the above findings. During breeding, MPAS exhibits the typical characteristics of rapid small-scale energy dissipation, sustained growth of large-scale energy, and migration of the spectral peak toward lower wavenumbers, consistent with atmospheric energy cascade theory. The PKE spectrum of FuXi consistently exhibits "flat-tail" or even "upturned" characteristics at small scales, indicating that it cannot effectively filter out small-scale noise and lacks the energy cascade mechanism from small to large scales. The rotational/divergent kinetic energy decomposition further reveals that FuXi primarily generates rotational kinetic energy at large scales, while its ability to capture divergent kinetic energy is extremely weak. This suggests that the bred perturbations mainly reflect the baroclinic instability of synoptic-scale vortex structures, whereas the representation of divergent processes such as convective instability is severely insufficient, consistent with the poor quality of FuXi perturbations and the dense noise in the low latitudes.

Although the above results reveal obvious deficiencies of FuXi in representing perturbation growth dynamics, including a lack of rapid initial response, difficulty in filtering out small-scale noise, missing energy cascade, and insufficient

representation of divergent motion, this does not imply that the bred perturbations cannot be used for ensemble forecasting. Success has already been achieved in AI-based ensemble forecasting using adjoint gradients, CNOP, or other methods[36-41], yet the perturbation generation process has not been studied in depth, and the perturbations obtained may primarily reflect mathematical response relationships in coarse-grained data rather than the full multiscale physical evolution. These findings suggest that when applying AI models to ensemble forecasting, attention should be paid not only to the final forecast outcomes but also to the perturbation generation process, thereby effectively improve the overall quality of ensemble perturbations. Future work could extend BGM to multiple AI models and larger samples, and incorporate more validation metrics, to further clarify the intrinsic mechanisms of perturbation growth dynamics in AI weather models.

## Methods

### MPAS

The numerical model employed in this study is the cross-scale global numerical weather prediction model MPAS-A (Model for Prediction Across Scales – Atmosphere) version 8.0.1, jointly developed by Los Alamos National Laboratory (LANL) and the National Center for Atmospheric Research (NCAR)[67]. This model is an advanced non-hydrostatic atmospheric model. The horizontal grid spacing is set to 24 km, close to the resolution of the FuXi model. Vertically, the model is configured with 55 layers, with the model top at 25 km. The physical parameterizations employ the New Tiedtke convection scheme, the WSM6 cloud microphysics scheme, the Noah land surface model, the YSU planetary boundary layer scheme, the Monin-Obukhov surface layer scheme, and the RRTMG longwave

and shortwave radiation transfer schemes.

**FuXi**

The FuXi model is a purely data-driven global weather forecasting model jointly developed by Fudan University and the Shanghai Academy of AI for Science, comprising a Cube Embedding module, a U-Transformer backbone, and fully connected prediction layers. The model is trained on 0.25°×0.25° ERA5 reanalysis data from 1979 to 2017, including geopotential height, temperature, meridional wind, zonal wind, and relative humidity at 13 isobaric levels, as well as five surface variables: 2-meter temperature, 10-meter zonal wind, 10-meter meridional wind, mean sea-level pressure, and 6-hour total precipitation[33].

The model achieves 0-5 day, 5-10 day, and 10-15 day forecasts through three cascaded models, namely FuXi-Short, FuXi-Medium, and FuXi-Long. This architecture is designed to minimize error accumulation from iterative predictions and to optimize performance across different forecast lead times. It extends the skillful lead time of deep-learning-based weather forecasting to 15 days for the first time, outperforming the ECMWF deterministic forecast at a 10-day lead time with 6-hourly temporal resolution and 0.25°×0.25° spatial resolution, and performing comparably to the ensemble mean of the ECMWF ensemble forecast at a 15-day lead time[68].

The model input consists of two initial states separated by 6 hours. Since the integration time step of BGM is set to 6 h, only the FuXi-Short model is used in this study.

**Breeding of Growing Modes (BGM)**

The Breeding of Growing Modes (BGM) method is one of the classical techniques for generating initial perturbations in ensemble forecasting. It was

proposed by Toth and Kalnay in the early 1990s and has been in operational use at the National Meteorological Center (NMC, now NCEP) since December 1992[9-11]. The core idea stems from observations of routine analysis cycles: in operational data assimilation systems, the differences between analysis fields and short-term forecasts naturally contain the rapidly growing error modes of the real atmosphere, the analysis cycle itself serves as a "breeding ground" for cultivating fast-growing modes. The BGM method explicitly simulates this natural process by introducing an additional perturbation forecast within the analysis cycle. After multiple cycles, fast-growing perturbations structurally similar to actual analysis errors are extracted and used as initial perturbations for ensemble forecasting (Fig. 9a)[11].

Fig. 9b presents a flow chart of the breeding cycle model with a 6-hour breeding period, described in detail as follows:

First, an initial perturbation $p_0$ is constructed as the initial mode. To represent the random errors in the initial field, the root-mean-square error (RMSE) $E_{p_0}(z)$ of each variable in the 24-hour model forecast is multiplied by a random number $R = (r_i)_N$. This random number follows a uniform distribution on $[-1,1]$, across all $N$ global grid points[59]. The initial mode of the breeding cycle is thus determined by:

$$p_0 = \omega R E_{p_0}(z), \tag{1}$$

where $\omega$ is the adjustment coefficient controlling the magnitude of the initial mode, with $E_{p_0}(z)$ defined as:

$$E_{p_0}(z) = \left(\frac{1}{N}\sum_{i=1}^{N} p_{0i}^2\right)^{1/2}. \tag{2}$$

Second, the initial perturbation $p_0$ is superimposed onto the control analysis field to form a perturbed initial field.

Then, the control forecast and the perturbed forecast are integrated forward

separately for 6 hours, and the difference between the two forecasts at the end of the cycle is computed as the output perturbation.

Finally, the perturbation field is rescaled to restore its magnitude to the level of the initial perturbation, superimposed onto the analysis field at the next time step, and proceeds to the next cycle. After several breeding cycles, the decaying components in the initial perturbation are gradually filtered out, while the fast-growing modes are preserved and tend toward saturation.

Let the perturbation field obtained at the end of the $t$-th breeding cycle (i.e., the output mode) be denoted as:

$$p_t' = f_t^p - f_t^c, \tag{3}$$

where $f_t^p$ is the perturbed forecast field and $f_t^c$ is the control forecast field. The dynamic adjustment coefficient is then defined as:

$$c_t = \frac{E_{p_0}}{E_{p_t'}}. \tag{4}$$

The magnitude of the output mode $E_{p_t'}$ can be calculated in exactly the same way as in Equation (2). Therefore, the input perturbation field for the next cycle (i.e., the input mode) is:

$$p_{t+1} = c_t p_t'. \tag{5}$$

Limited by computational resources, the experiments in this paper use 12:00 UTC on 26 March 2025 as the initial time of the breeding cycle.

**Perlin noise**

Perlin noise is a gradient noise generation algorithm proposed by Ken Perlin[69-71], designed to generate pseudo-random signals with finite bandwidth, isotropy, and spatial continuity. Unlike white noise, whose power spectrum is uniform, Perlin

noise concentrates energy within a finite frequency band and exhibits smooth transitions between adjacent points, thereby more closely mimicking natural random phenomena[72]. Its generation process involves assigning pseudo-random gradient vectors at regular lattice vertices and computing noise values at any point within the lattice through smooth interpolation. A multi-fractal extension superimposes components at multiple octaves, expressed as:

$$f(\mathbf{x}) = \sum_{i=0}^{n-1} p^i \cdot \mathcal{N}\left(2^i \cdot \mathrm{s} \cdot \mathbf{x}\right), \tag{6}$$

where $\mathbf{x}$ is the spatial coordinate; $s$ (scale) is the frequency scaling factor that determines the characteristic spatial scale of the perturbation field. Increasing $s$ shifts energy toward higher wavenumbers, generating finer, more fragmented small-scale perturbations; conversely, a smaller $s$ produces smoother, larger-scale structures. $n$ (octaves) is the number of octaves, controlling the total number of frequency layers; each additional layer introduces detail at double the spatial frequency, transitioning the field from a single scale to a multi-scale structure. $p$ (persistence) is the amplitude decay factor regulating energy distribution across scales: when $p > 1$, high frequencies dominate and the field appears rough and fragmented; when $p < 1$, low frequencies dominate and the field tends to be smooth; when $p = 1$, amplitudes across frequency bands are equal. Together, these three parameters determine the effective spatial correlation length and spectral slope of the perturbation field.

The physical meaning of the Perlin noise parameters is explicit, so no historical samples are required to generate isotropic, spatially continuous perturbation fields. Its scale tunability ensures coverage of multi-scale instability modes, facilitating the investigation of the influence of different initial field structures on breeding results.

**Measures of Perturbation Saturation**

***Measure of perturbation magnitude saturation***

The measure of perturbation magnitude saturation generally examines the magnitude of the perturbation growth rate, defined as:

$$r_t = \frac{E_{p_t}}{E_{p_{t-1}}}, \tag{7}$$

where $E_{p_t}$ represents the perturbation growth mode magnitude after the $t$-th cycle.

The perturbation growth rate is a key indicator measuring the speed of perturbation development. For perturbations that make practical contributions to ensemble forecasting, they should essentially be fast-growing modes. During the breeding cycle, non-growing or decaying components in the initial perturbation will be gradually filtered out, and only the fast-growing components will ultimately be retained. Correspondingly, the perturbation growth rate will rapidly increase, then gradually decrease, and finally approach 1.0. At this point, the perturbation is considered to have reached saturation, and this stable value is called the saturation growth rate[9].

***Measure of perturbation morphology saturation***

Examining the saturation of perturbation morphology involves assessing the similarity between two perturbation fields before and after each breeding step. The simplest method for judging the similarity between two physical quantity fields is to calculate the similarity coefficient between them. Therefore, for measuring perturbation morphology saturation in the breeding cycle, the following two quantities can be calculated:

Sign index:

$$s_{ij} = \frac{n^+ - n^-}{n^+ + n^-}, \tag{8}$$

where $n^+$ is the number of grid points with the same sign of anomaly between the two samples, and $n^-$ is the number of grid points with opposite signs.

Pearson correlation coefficient:

$$\rho_{ij} = \frac{\sum_{k=1}^{N}(x_{ik}-\bar{x}_i)(x_{jk}-\bar{x}_j)}{\sqrt{\sum_{k=1}^{N}(x_{ik}-\bar{x}_i)^2 \cdot \sum_{k=1}^{N}(x_{jk}-\bar{x}_j)^2}}. \quad (9)$$

When the perturbation field obtained after a breeding step is very similar to the perturbation field before that step, it indicates that the morphology of the perturbation growth mode has tended to saturate, and the breeding cycle can be terminated.

## Perturbation Kinetic Energy (PKE) Spectrum

This study uses spherical harmonic function decomposition to compute the horizontal perturbation kinetic energy (PKE) spectrum[63,64]. For a given horizontal perturbation wind field $\mathbf{V}' = (u', v')$, the perturbation kinetic energy per unit mass is defined as:

$$PKE = \frac{1}{2}(u'^2 + v'^2). \quad (10)$$

The wind field is decomposed via the Helmholtz theorem into rotational and divergent components:

$$\mathbf{V}' = -\nabla \times (\psi' \hat{\mathbf{r}}) + \nabla \chi', \quad (11)$$

where $\psi'$ is the perturbation streamfunction, $\chi'$ is the perturbation velocity potential, and $\hat{\mathbf{r}}$ denotes the radial unit vector pointing in the Earth's radial direction (i.e., vertical). The vertical vorticity $\zeta'$ and horizontal divergence $D'$ relate to the streamfunction and velocity potential by $\zeta' = \nabla^2 \psi'$ and $D' = \nabla^2 \chi'$.

The spectral coefficients ${\zeta'}_{lm}$ and ${D'}_{lm}$ of vorticity and divergence are obtained

by spherical harmonic transform. The rotational kinetic energy spectrum and divergent kinetic energy spectrum at total wavenumber $l$ are computed respectively as:

$$PKE_{rot}^{lm} = \frac{a^2}{2l(l+1)}(\zeta', \zeta')_{lm}, \tag{12}$$

$$PKE_{div}^{lm} = \frac{a^2}{2l(l+1)}(D', D')_{lm}. \tag{13}$$

The total kinetic energy spectrum is the sum of the two:

$$PKE^{lm} = PKE_{rot}^{lm} + PKE_{div}^{lm}. \tag{14}$$

Where $a$ is the Earth's radius, $m$ is the zonal wavenumber. This spectral analysis method provides a quantitative measure of the energy distribution across different spatial scales, enabling analysis of the multi-scale energy evolution characteristics of perturbation fields[65,66].

## References


1. Mu, M., Qin, B. & Dai, G. K. Predictability study of weather and climate events related to artificial intelligence models. *Adv. Atmos. Sci.* **42**, 1–8 (2025). https://doi.org/10.1007/s00376-024-4372-7
2. Lorenz, E. N. Deterministic nonperiodic flow. *J. Atmos. Sci.* **20**, 130–141 (1963). https://doi.org/10.1175/1520-0469(1963)020<0130:DNF>2.0.CO;2
3. Lorenz, E. N. The predictability of a flow which possesses many scales of motion. *Tellus* **21**, 289–307 (1969). https://doi.org/10.1111/j.2153-3490.1969.tb00444.x
4. Lorenz, E. N. A study of the predictability of a 28-variable atmospheric model. *Tellus* **17**, 321–333 (1965). https://doi.org/10.1111/j.2153-3490.1965.tb01424.x

5. Lorenz, E. N. Predictability: does the flap of a butterfly's wings in Brazil set off a tornado in Texas? in Section on Environmental Sciences: New Approaches to Global Weather, 139th Annual Meeting of the American Association for the Advancement of Science (AAAS, Washington DC, 1972).
6. Zhu, Y. J., Dai, K. & Tang, J. Reducing forecast uncertainty and improving forecast capability——Development and application of ensemble forecast (in Chinese). *Meteorological Monthly.* **51**, 1335–1352 (2025). https://doi.org/10.7519/j.issn.1000-0526.2025.091801
7. Chen, J. et al. A review on development, challenges, and future perspectives of ensemble forecast (in Chinese). *Acta Meteorologica Sinica.* **83**, 480–502 (2025). https://doi.org/10.11676/qxxb2025.20240151
8. Epstein, E. S. Stochastic dynamic prediction. *Tellus* **21**, 739–759 (1969). https://doi.org/10.1111/j.2153-3490.1969.tb00483.x
9. Toth, Z. & Kalnay, E. Ensemble forecasting at NMC: the generation of perturbations. *Bull. Am. Meteorol. Soc.* **74**, 2317–2330 (1993). https://doi.org/10.1175/1520-0477(1993)074<2317:EFANTG>2.0.CO;2
10. Toth, Z. & Kalnay, E. Ensemble forecasting at NMC and the breeding method. NOAA/NCEP Office Note 403 (NOAA, 1995).
11. Toth, Z. & Kalnay, E. Ensemble forecasting at NCEP and the breeding method. *Mon. Weather Rev.* **125**, 3297–3319 (1997). https://doi.org/10.1175/1520-0493(1997)125<3297:EFANAT>2.0.CO;2
12. Buizza, R. Potential forecast skill of ensemble prediction, and spread and skill distributions of the ECMWF Ensemble Prediction System. *Mon. Weather Rev.* **125**, 99–119 (1997). https://doi.org/10.1175/1520-0493(1997)125<0099:PFSOEP>2.0.CO;2

13. Buizza, R., Tribbia, J., Molteni, F. & Palmer, T. Computation of optimal unstable structures for a numerical weather prediction model. *Tellus A* **45**, 388–407 (1993). https://doi.org/10.3402/tellusa.v45i5.14901
14. Molteni, F., Buizza, R., Palmer, T. N. & Petroliagis, T. The ECMWF ensemble prediction system: methodology and validation. *Q. J. R. Meteorol. Soc.* **122**, 73–119 (1996). https://doi.org/10.1002/qj.49712252905
15. Evensen, G. Sequential data assimilation with a nonlinear quasi-geostrophic model using Monte Carlo methods to forecast error statistics. *J. Geophys. Res. Oceans* **99**, 10143–10162 (1994). https://doi.org/10.1029/94JC00572
16. Houtekamer, P. L. & Mitchell, H. L. Data assimilation using an ensemble Kalman filter technique. *Mon. Weather Rev.* **126**, 796–811 (1998). https://doi.org/10.1175/1520-0493(1998)126<0796:DAUAEK>2.0.CO;2
17. Isaksen, L., Bonavita, M., Buizza, R., Fisher, M., Haseler, J., Leutbecher, M. & Raynaud, L. Ensemble of data assimilations at ECMWF. ECMWF Technical Memorandum No. 636 (ECMWF, 2010). https://www.ecmwf.int/node/9425
18. Ling, F. et al. Improving global weather and ocean wave forecast with large artificial intelligence models. *Sci. China Earth Sci.* **67**, 3641–3654 (2024). https://doi.org/10.1007/s11430-024-1452-3
19. Liu, C.-C. et al. Evaluation of five global AI models for predicting weather in eastern Asia and western Pacific. *npj Clim. Atmos. Sci.* **7**, 221 (2024). https://doi.org/10.1038/s41612-024-00769-0
20. Luo, J.-J. et al. AI for atmosphere–ocean sciences: advancements, challenges and ways forward. *Natl. Sci. Rev.* **13**, nwag063 (2026). https://doi.org/10.1093/nsr/nwag063
21. Mu, M., Qin, B. & Dai, G. A commentary of “Artificial intelligence models bring new breakthroughs in global accurate weather forecasting”: top 10

606 scientific advances of 2023, China. *Fundam. Res.* **4**, 690–692 (2024).
607 https://doi.org/10.1016/j.fmre.2024.03.006
608 22. Zhang, F., Huang, X., Mu, M., Qin, B. & Li, J. Large AI models: pioneering
609 innovations in accurate weather forecasting. *Chin. Sci. Bull.* **69**, 5016–5019
610 (2024). https://doi.org/10.1360/TB-2024-0543
611 23. Pathak, J. et al. FourCastNet: a global data-driven high-resolution weather model
612 using adaptive Fourier neural operators. Preprint at
613 https://doi.org/10.48550/arXiv.2202.11214 (2022).
614 24. Bi, K., Xie, L., Zhang, H., Chen, X., Gu, X. & Tian, Q. Accurate medium-range
615 global weather forecasting with 3D neural networks. *Nature* **619**, 533–538
616 (2023). https://doi.org/10.1038/s41586-023-06185-3
617 25. Zhang, Y., Long, M., Chen, K., Zhang, X., Wang, Y. & Yi, P. Skilful nowcasting
618 of extreme precipitation with NowcastNet. *Nature* **619**, 526–532 (2023).
619 https://doi.org/10.1038/s41586-023-06184-4
620 26. Gao, Y. et al. OneForecast: a universal framework for global and regional
621 weather forecasting. Preprint at https://doi.org/10.48550/arXiv.2502.00338
622 (2025).
623 27. Nguyen, T., Brandstetter, J., Kapoor, A., Gupta, J. K. & Grover, A. ClimaX: a
624 foundation model for weather and climate. in *Proceedings of the 40th*
625 *International Conference on Machine Learning, PMLR* **202**, 25904–25929
626 (2023). https://proceedings.mlr.press/v202/nguyen23a.html
627 28. Lam, R. et al. Learning skillful medium-range global weather forecasting.
628 *Science* **382**, 1416–1421 (2023). https://doi.org/10.1126/science.adi2336
629 29. Price, I. et al. Probabilistic weather forecasting with machine learning. *Nature*
630 **637**, 84–90 (2024). https://doi.org/10.1038/s41586-024-08252-9
631 30. Kochkov, D. et al. Neural general circulation models for weather and climate.
632 *Nature* **632**, 1060–1066 (2024). https://doi.org/10.1038/s41586-024-07744-y

31. Chen, K. et al. The operational medium-range deterministic weather forecasting can be extended beyond a 10-day lead time. *Commun. Earth Environ.* **6**, 518 (2025). https://doi.org/10.1038/s43247-025-02502-y
32. Lang, S. et al. AIFS–ECMWF's data-driven forecasting system. Preprint at https://doi.org/10.48550/arXiv.2406.01465 (2024).
33. Chen, L., Zhong, X., Zhang, F. et al. FuXi: a cascade machine learning forecasting system for 15-day global weather forecast. *npj Clim. Atmos. Sci.* **6**, 190 (2023). https://doi.org/10.1038/s41612-023-00512-1
34. Yuan, S., Wang, G., Mu, B. & Zhou, F. TianXing: a linear complexity transformer model with explicit attention decay for global weather forecasting. *Adv. Atmos. Sci.* **42**, 9–25 (2025). https://doi.org/10.1007/s00376-024-3313-9
35. Liu, X. et al. Global ensemble weather prediction from a deep learning-based model (Pangu-Weather) with the initial condition perturbations of CMA-GEPS. *Adv. Atmos. Sci.* **42**, 1636–1660 (2025). https://doi.org/10.1007/s00376-024-4173-z
36. Baño-Medina, J., Sengupta, A., Doyle, J. D., Reynolds, C. A. & Watson-Parris, D. Are AI weather models learning atmospheric physics? A sensitivity analysis of cyclone Xynthia. *npj Clim. Atmos. Sci.* **8**, 92 (2025). https://doi.org/10.1038/s41612-025-00949-6
37. Pu, J., Mu, M., Feng, J., Zhong, X. & Li, H. A fast physics-based perturbation generator of machine learning weather model for efficient ensemble forecasts of tropical cyclone track. *npj Clim. Atmos. Sci.* **8**, 128 (2025). https://doi.org/10.1038/s41612-025-01009-9
38. Zhou, Z., Duan, W., Yang, R., Qin, X. & Li, Y. Uncertainty of Pangu-Weather in Bay of Bengal storm track forecasts: target observation perspective. *Atmos. Res.* **326**, 108313 (2025). https://doi.org/10.1016/j.atmosres.2025.108313

659 39. Guo, A., Mu, M., Qin, B., Pu, J. & Li, H. A nonlinear explainable method for
660 data-driven forecasting models in Earth system science. *npj Clim. Atmos. Sci.*
661 (2026). https://doi.org/10.1038/s41612-026-01464-y
662 40. Pu, J., Mu, M., Feng, J. & Li, H. Error growth dynamics and predictability of
663 tropical cyclones in machine-learning weather prediction models. *Q. J. R.*
664 *Meteorol. Soc.* (2026). https://doi.org/10.1002/qj.70257
665 41. Li, Y., Duan, W., Han, W., Li, H. & Qin, X. Improving tropical cyclone track
666 forecast skill through assimilating target observation achieved by AI-based
667 conditional nonlinear optimal perturbation. *J. Geophys. Res. Atmos.* **130**,
668 e2024JD043261 (2025). https://doi.org/10.1029/2024JD043261
669 42. Guardamagna, F., Wieners, C. & Dijkstra, H. A. Explaining the high skill of
670 reservoir computing methods in El Niño prediction. *Nonlinear Process. Geophys.*
671 **32**, 201–224 (2025). https://doi.org/10.5194/npg-32-201-2025
672 43. Zhou, L., Zhang, R.-H. & Tao, L. AI-enabled conditional nonlinear optimal
673 perturbation enhances ensemble prediction of extreme El Niño events. *npj Clim.*
674 *Atmos. Sci.* **9**, 30 (2025). https://doi.org/10.1038/s41612-025-01303-6
675 44. Ji, C., Y. Wei, B. Qin, M. Mu & H. Ren, 2026: MJO Initiation Predictability in
676 an AI-CNOP Framework: Unraveling Precursor Signals of Primary MJO
677 Events. *Adv. Atmos. Sci*., https://doi.org/10.1007/s00376-026-6133-2
678 45. Leung, J. C.-H., D.-S. Xu, W.-Y. Yu, S.-J. Zhang, X.-D. Zeng, G.-Z. Nie, J.
679 Feng, J.-C. Pu, Y. Li, K.-J. Ren, Q.-C. Zeng & B.-L. Zhang, 2026: Butterfly
680 Effect Confirmed in Global AI Weather Models: Evidence from Tropical
681 Cyclone Forecasting. *arXiv preprint*, arXiv:2609.39379.
682 46. Sun, Y. Q., Hassanzadeh, P., Zand, M., Chattopadhyay, A., Weare, J. & Abbot,
683 D. S. Can AI weather models predict out-of-distribution gray swan tropical
684 cyclones? *Proc. Natl. Acad. Sci. U.S.A.* **122**, e2420914122
685 (2025). https://doi.org/10.1073/pnas.2420914122

47. Sun, Y. Q., Hassanzadeh, P., Shaw, T., Pahlavan, H. A. & Marchakitus, A. Predicting regional gray swans via translocation: AI weather models and Dubai's unprecedented 2024 rainfall. *Sci. Adv.* **12**, eady9406 (2026). https://doi.org/10.1126/sciadv.ady9406

48. Zhang, Z., Fischer, E., Zscheischler, J. & Engelke, S. Physics-based models outperform AI weather forecasts of record-breaking extremes. *Sci. Adv.* **12**, eaec1433 (2026). https://doi.org/10.1126/sciadv.aec1433

49. Chattopadhyay, A., Sun, Y. Q. & Hassanzadeh, P. Challenges of learning multi-scale dynamics with AI weather models: Implications for stability and one solution. arXiv, arXiv:2304.07029 (2023). https://doi.org/10.48550/arXiv.2304.07029

50. Selz, T. & Craig, G. C. Can artificial intelligence-based weather prediction models simulate the butterfly effect? *Geophys. Res. Lett.* **50**, e2023GL105747 (2023). https://doi.org/10.1029/2023GL105747

51. Bonavita, M. On some limitations of current machine learning weather prediction models. *Geophys. Res. Lett.* **51**, e2023GL107377 (2024). https://doi.org/10.1029/2023GL107377

52. Selz, T. & Craig, G. C. Can AI-based weather prediction models simulate the butterfly effect? The role of architecture and implementation. *J. Geophys. Res. Mach. Learn. Comput.* **3**, e2025JH001180 (2026). https://doi.org/10.1029/2025JH001180

53. Kim, H., Ryu, J., Son, S.-W., Jeong, J.-H., Kim, H. & Yoon, J.-H. A spectral test of the butterfly effect and physical consistency in the diffusion-based GenCast's ensembles. *npj Clim. Atmos. Sci.* **9**, 110 (2026). https://doi.org/10.1038/s41612-026-01380-1

54. Chen, J.-K., Oskarsson, J., Driscoll, S. & Schemm, S. Butterfly Effect and the Kinetic Energy Cascade in Probabilistic Machine Learning Weather Prediction Models. *arXiv preprint*, arXiv:2609.18489 (2026).
55. Hassanzadeh, P., Li, W., Sun, Y. Q., Wang, J., Wikner, A., Finkel, J. & Weare, J. Q. Missing the Butterfly and Predicting the Past: Features or Bugs of Accurate AI Weather Models? *arXiv*, arXiv:2608.25835 (2026). https://doi.org/10.48550/arXiv.2608.25835
56. Kalnay, E. Atmospheric predictability and ensemble forecasting. in *Earth System Modeling, Data Assimilation and Predictability* (eds E. Kalnay, S. Mote & C. Da) Ch. 6, 224–282 (Cambridge University Press, 2024). https://doi.org/10.1017/9780511920608.006
57. Yu, Y. & L. Zhang. A Study of Initial Perturbation Saturation in Ensemble Prediction Based on the "Breeding of Growing Modes" Method (in Chinese). *Chin. J. Atmos. Sci.* **29**, 955–964 (2005). https://doi.org/10.3878/j.issn.1006-9895.2005.06.11
58. Yu, Y., L. Zhang & Y. Luo. The Breeding of Growing Modes with Dynamic Rescaling in Ensemble Prediction and Improvement on Free Breeding (in Chinese). *Chin. J. Atmos. Sci.* **31**, 527–535 (2007). https://doi.org/10.3878/j.issn.1006-9895.2007.03.16
59. Guan, J., Huang, H. & Zhang, L. Methods of producing initial perturbations in ensemble forecast (in Chinese). *J. PLA Univ. Sci. Technol.* **4**, 87–90 (2003).
60. Liu, J., L. Zhang, N. Mei & L. Li. Analysis and Study of the Growth Mode Breeding Developing in the Tropical Areas (in Chinese). *J. Trop. Meteorol.* **28**, 104–112 (2012). https://doi.org/10.3969/j.issn.1004-4965.2012.01.012
61. Skamarock, W. C., Park, S.-H., Klemp, J. B. & Snyder, C. Atmospheric kinetic energy spectra from global high-resolution nonhydrostatic simulations. *J. Atmos. Sci.* **71**, 4369–4381 (2014). https://doi.org/10.1175/JAS-D-14-0114.1

62. Selz, T., Bruinsma, W., Craig, G., Markou, S., Turner, R. & Vaughan, A. On the effective resolution of AI weather models. in EMS Annual Meeting 2025 (European Meteorological Society, 2025). https://doi.org/10.5194/ems2025-541
63. Ehrendorfer, M. *Spectral Numerical Weather Prediction Models* (Society for Industrial and Applied Mathematics, Philadelphia, PA, 2011). https://doi.org/10.1137/1.9781611971996
64. Holmes, S. A. & Featherstone, W. E. A unified approach to the Clenshaw summation and the recursive computation of very high degree and order normalised associated Legendre functions. *J. Geod.* **76**, 279–299 (2002). https://doi.org/10.1007/s00190-002-0216-2
65. Nastrom, G. D. & Gage, K. S. A climatology of atmospheric wavenumber spectra of wind and temperature observed by commercial aircraft. *J. Atmos. Sci.* **42**, 950–960 (1985). https://doi.org/10.1175/1520-0469(1985)042<0950:ACOAWS>2.0.CO;2
66. Li, Z., Peng, J. & Zhang, L. Spectral budget of rotational and divergent kinetic energy in global analyses. *J. Atmos. Sci.* **80**, 813–831 (2023). https://doi.org/10.1175/JAS-D-21-0332.1
67. Skamarock, W. C., Klemp, J. B., Duda, M. G., Fowler, L. D., Park, S.-H. & Ringler, T. D. A multiscale nonhydrostatic atmospheric model using centroidal Voronoi tesselations and C-grid staggering. *Mon. Weather Rev.* **140**, 3090–3105 (2012). https://doi.org/10.1175/MWR-D-11-00215.1
68. Huang, X., Y. Lin, W. Xiong, J. Li, J. Pan & Y. Zhou. Research on international developments of AI large meteorological models in numerical forecasting (in Chinese). *Trans. Atmos. Sci.* **47**, 46–54 (2024). https://doi.org/10.13878/j.cnki.dqkxxb.20231201001.
69. Perlin, K. An image synthesizer. *Comput. Graph.* **19**, 287–296 (1985). https://doi.org/10.1145/325165.325247

70. Perlin, K. Improving noise. *ACM Trans. Graph.* **21**, 681–682 (2002). https://doi.org/10.1145/566654.566636
71. Perlin, K. Implementing improved Perlin noise. in *GPU Gems: Programming Techniques, Tips, and Tricks for Real-Time Graphics* (ed. Randima Fernando) Ch. 5 (Addison-Wesley Professional, 2004).
72. Li, J., X. He, Y. Liu, F. Meng & Q. Zhu. A Procedural Texture Synthesis Method Based on Perlin Noise and Fractal Brownian Motion (in Chinese). J. *Chengdu Univ. Inf. Technol.* **40**, 14–20 (2025). https://doi.org/10.16836/j.cnki.jcuit.2025.01.003

## Data Availability

ERA5 reanalysis data are publicly available from the Copernicus Climate Data Store https://cds.climate.copernicus.eu/. The FuXi model is open-sourced at https://github.com/tpys/FuXi. The MPAS-A (Model for Prediction Across Scales – Atmosphere) version 8.0.1 model code is publicly available at https://github.com/MPAS-Dev/MPAS-Model.

## Acknowledgements

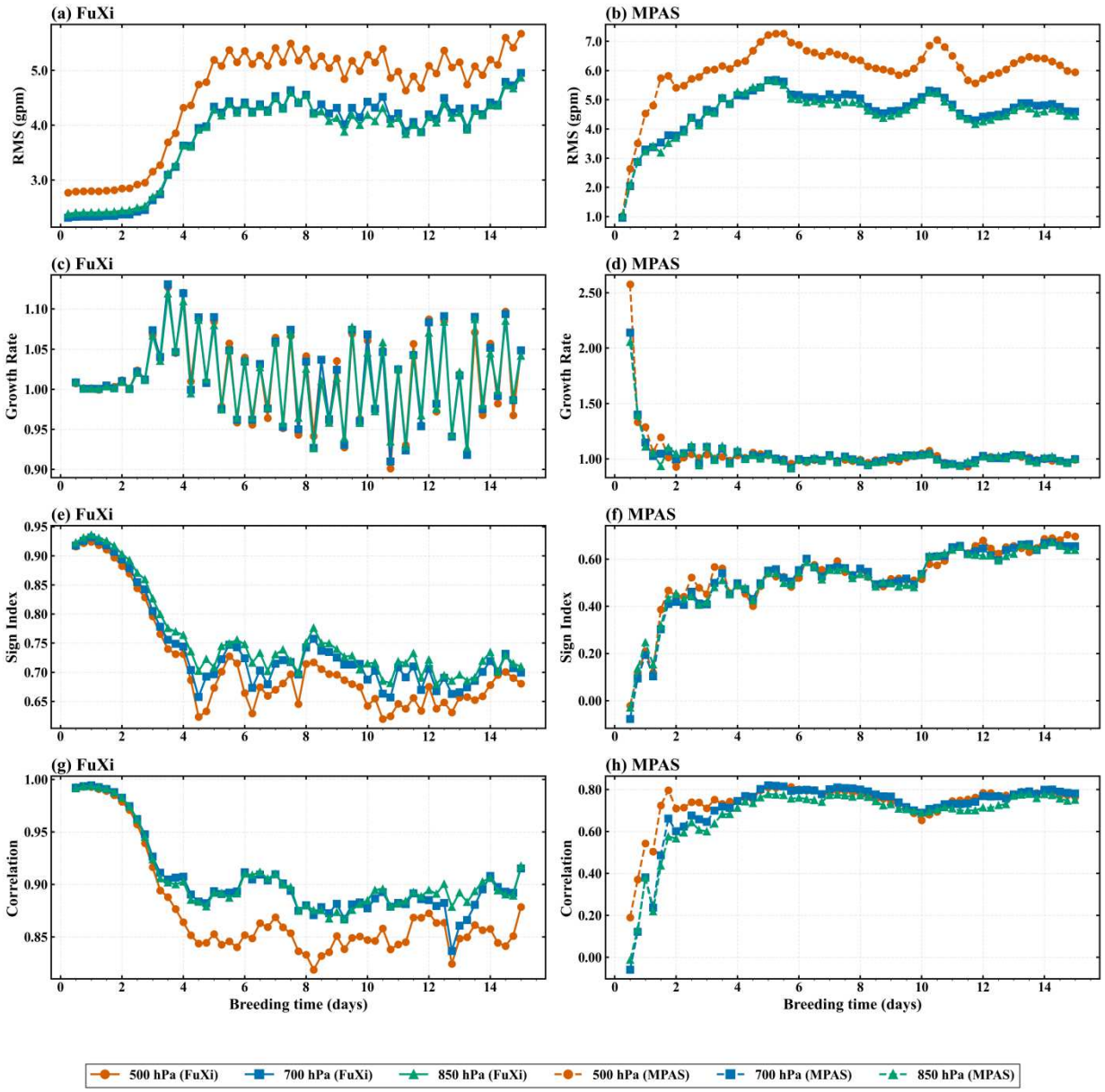
This research was funded by the National Key Research and Development Program of China, grant number 2025YFF0517201, and the National Natural Science Foundation of China, grant number 42575071, 42422503, and 42275062. We appreciate the developers of the FuXi and MPAS models for their efforts in building and maintaining these open-source tools, without which this study would not have been feasible.

## Author contributions

X.S. and J.G. designed the research. X.S. and C.L. performed the experiments and analyzed the data. X.S. and C.L. wrote the manuscript. J.P., J.G. and L.Z. contributed to the interpretation of results and manuscript revision. All authors have read and approved the manuscript.

## Competing interests

The authors declare no competing financial or non-financial interests.




798

799 **Fig. 1 | Evolution curves of geopotential height perturbations at 500 hPa, 700**
800 **hPa, and 850 hPa during the breeding cycle**. left column (**a, c, e, g**) shows FuXi,
801 right column (**b, d, f, h**) shows MPAS. From top to bottom are the perturbation field
802 RMS (**a, b**), perturbation growth rate (**c, d**), sign index (**e, f**), and Pearson correlation
803 coefficient (**g, h**).

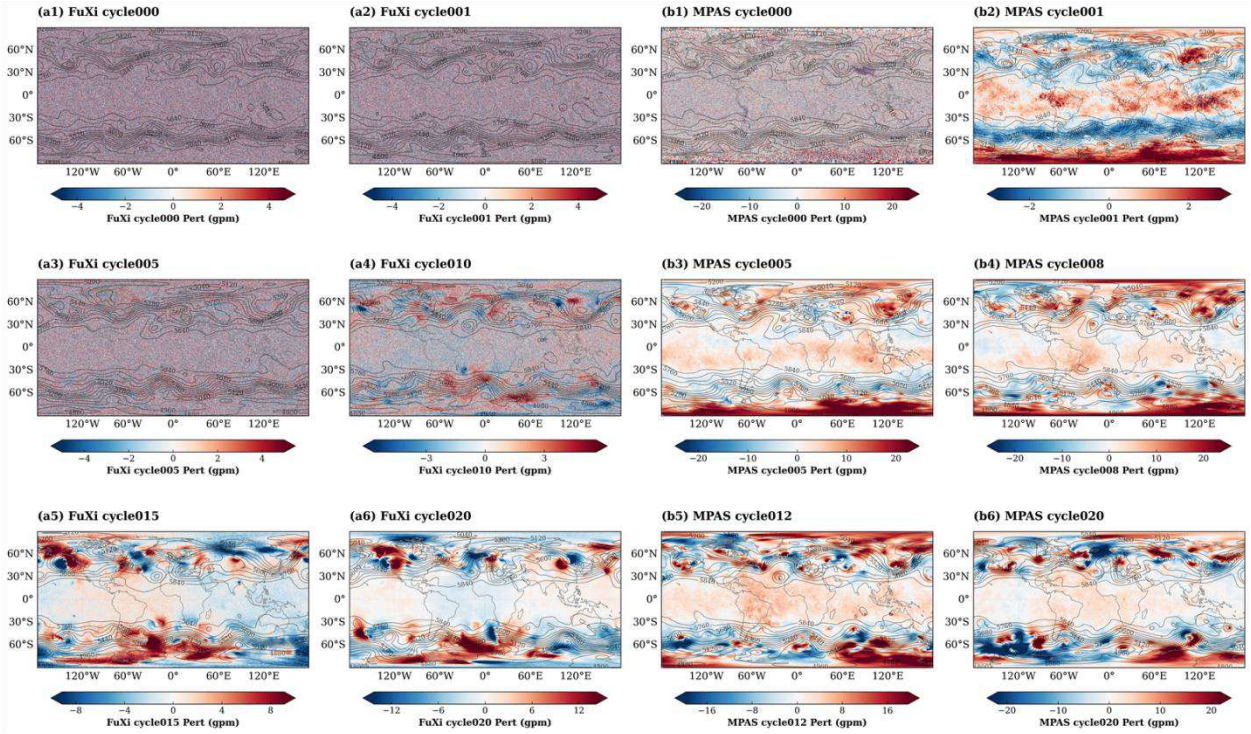



**Fig. 2 | Spatial distribution of 500 hPa geopotential height perturbation fields (shaded) and the corresponding ERA5 analysis geopotential heights (contours) during the breeding cycle.** The two left columns (**a1–a6**) show FuXi, the right column (**b1–b6**) shows MPAS. The specific cycle numbers are indicated in the subplot titles, representing different stages of the breeding process.

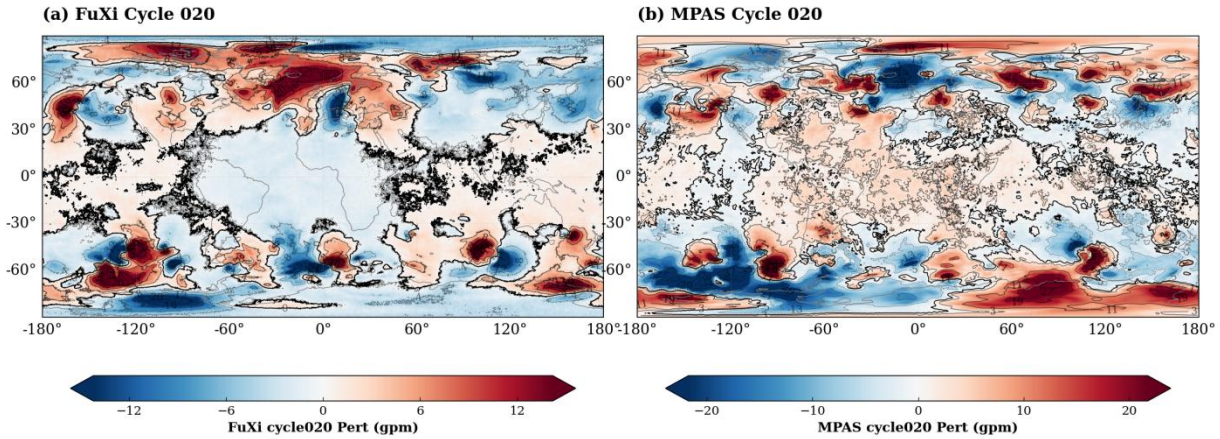
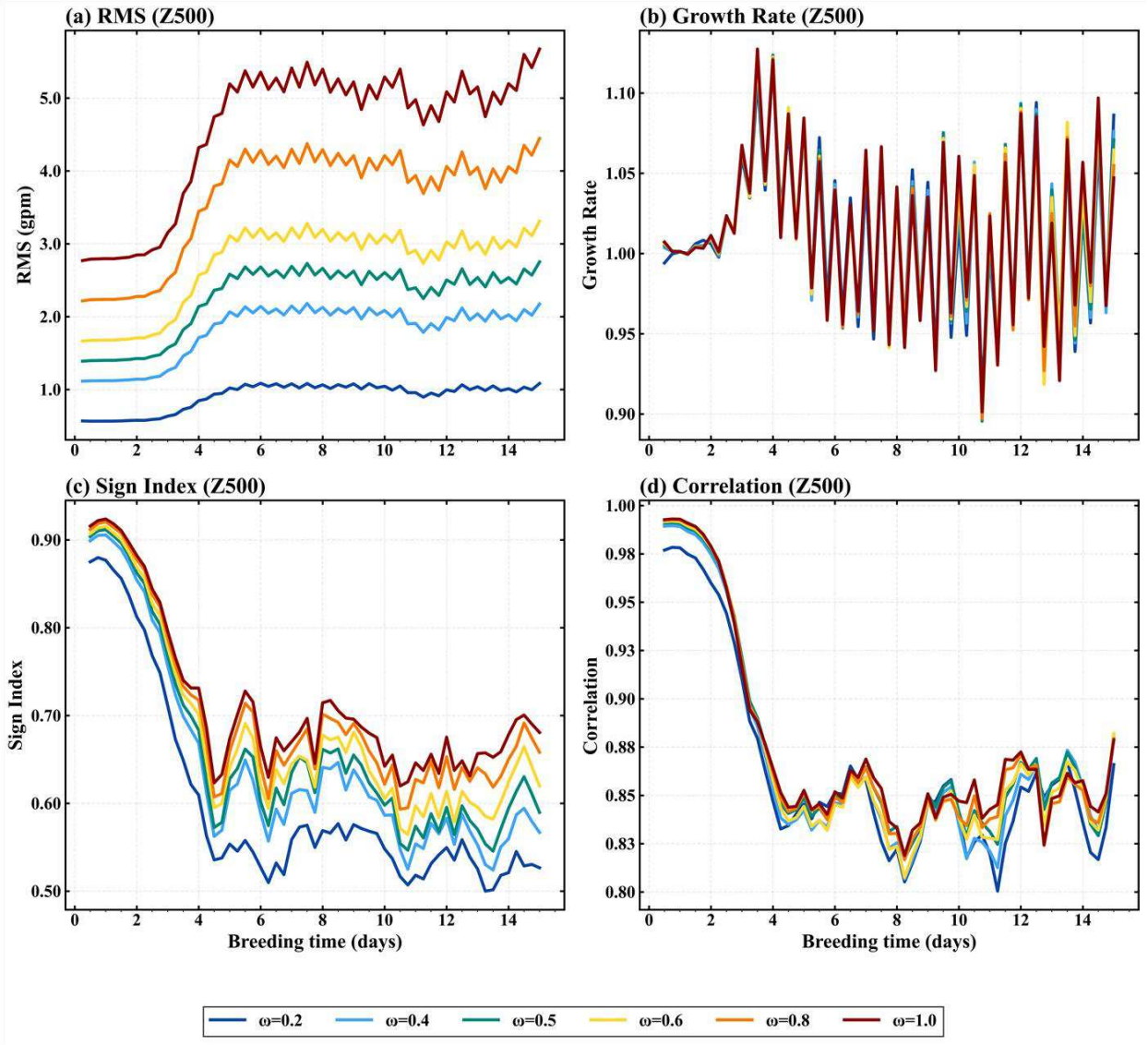


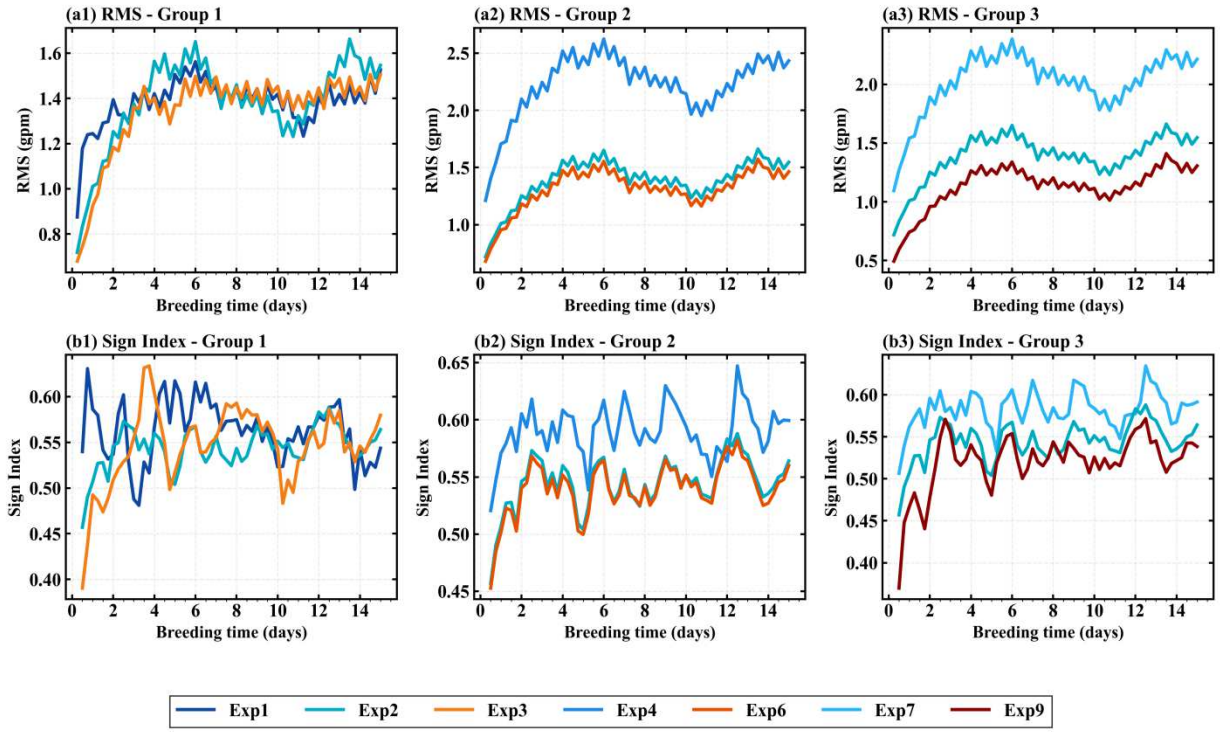

**Fig. 3 | Spatial distribution of the 500 hPa geopotential height saturated perturbation field (shaded).** (**a**) FuXi, (**b**) MPAS. The output of the 20th breeding cycle is shown as an example.




815

816 **Fig. 4 | Evolution curves of 500 hPa geopotential height perturbation breeding**
817 **cycles for different *ω* values**. (**a**) RMS, (**b**) perturbation growth rate, (**c**) sign index,
818 (**d**) Pearson correlation coefficient.

819




820

821 **Fig. 5 | Evolution curves of 500 hPa geopotential height perturbation breeding**
822 **cycles for different Perlin noise parameters:** (**a**) RMS, (**b**) sign index. left column
823 is Group 1, middle column is Group 2, right column is Group 3.

824

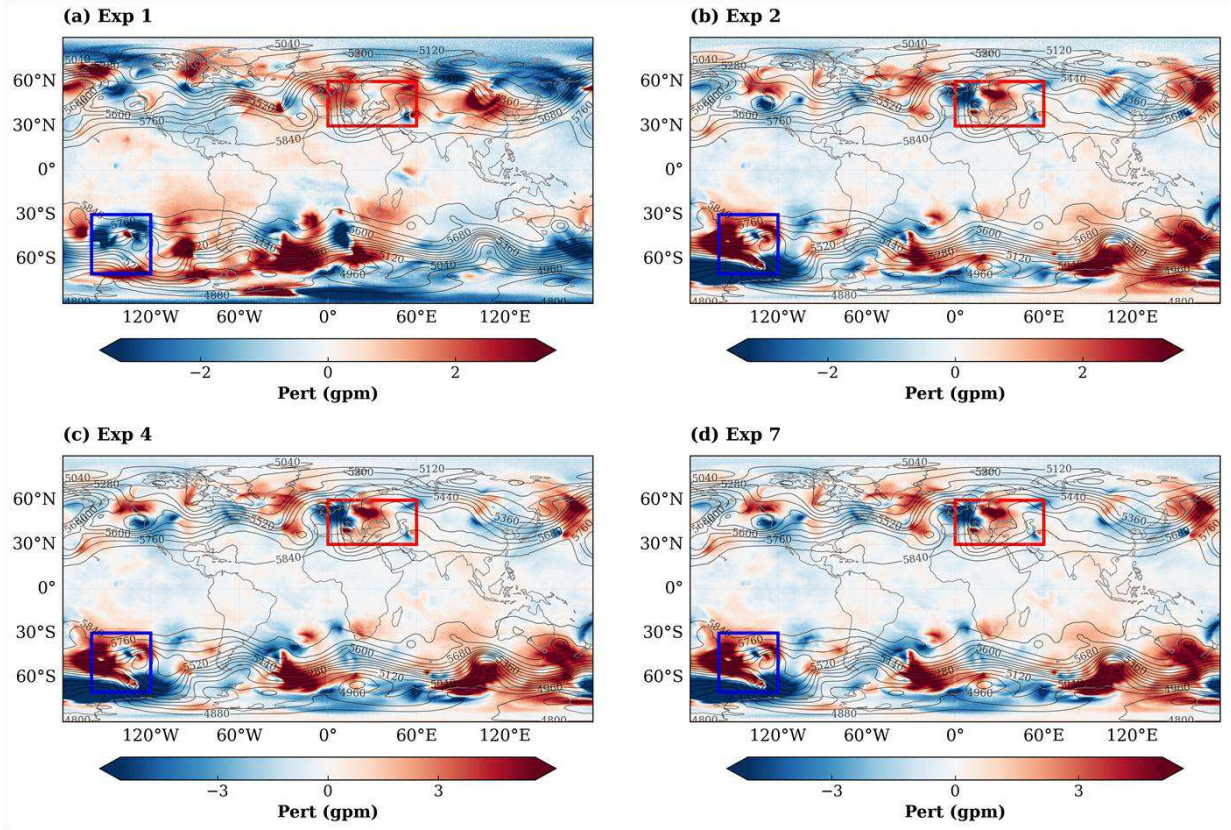
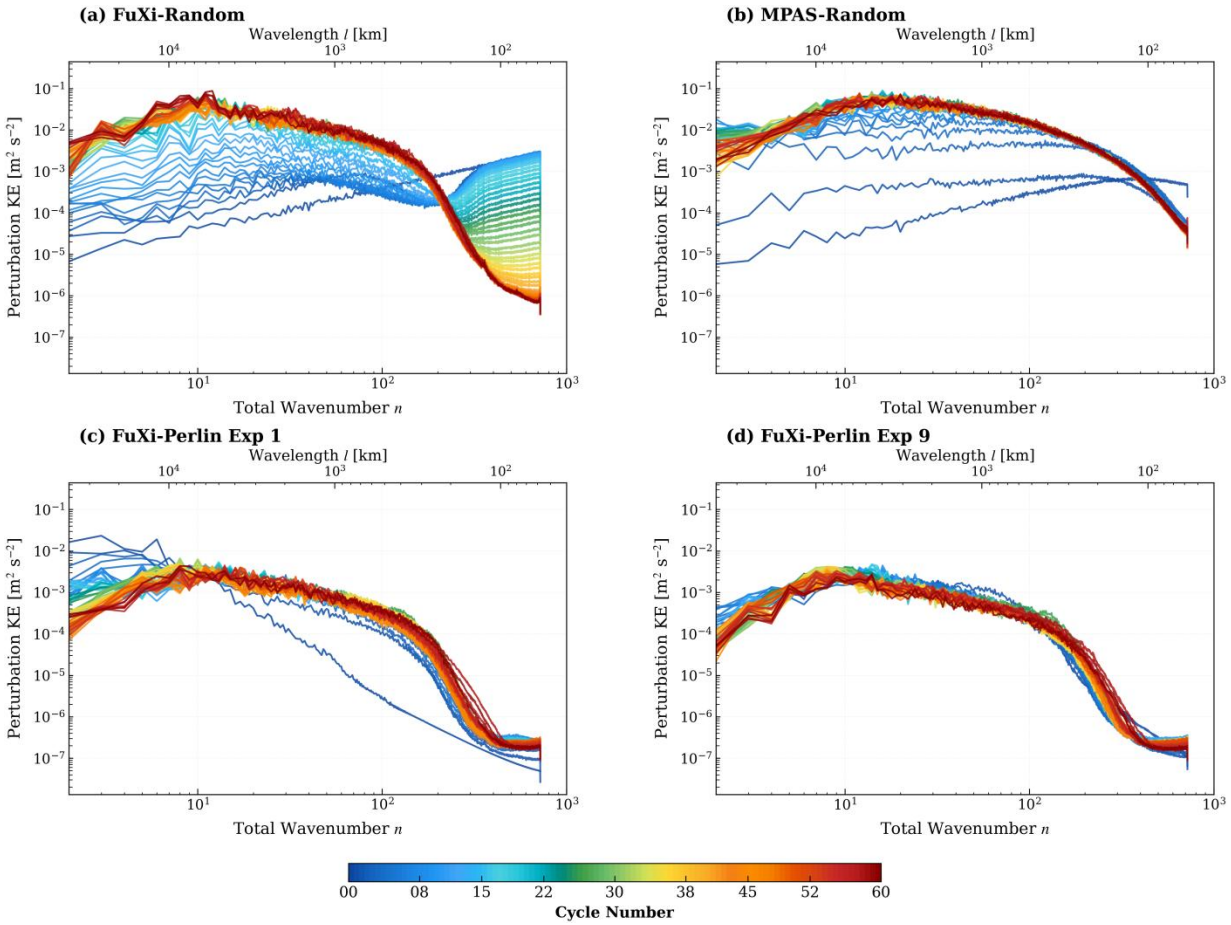



**Fig. 6 | Spatial distributions of 500 hPa geopotential height saturated perturbations for different Perlin noise parameters:** (**a**) Exp 1, (**b**) Exp 2, (**c**) Exp 4, (**d**) Exp 7.




830

831 **Fig. 7 | Evolution of the 500 hPa perturbation kinetic energy spectrum during**
832 **the breeding cycle.** (**a**) FuXi random-number field, (**b**) MPAS random-number field;
833 (**c**) FuXi Perlin noise Exp 1, (**d**) FuXi Perlin noise Exp 9. Different colors represent
834 different cycle numbers.

835

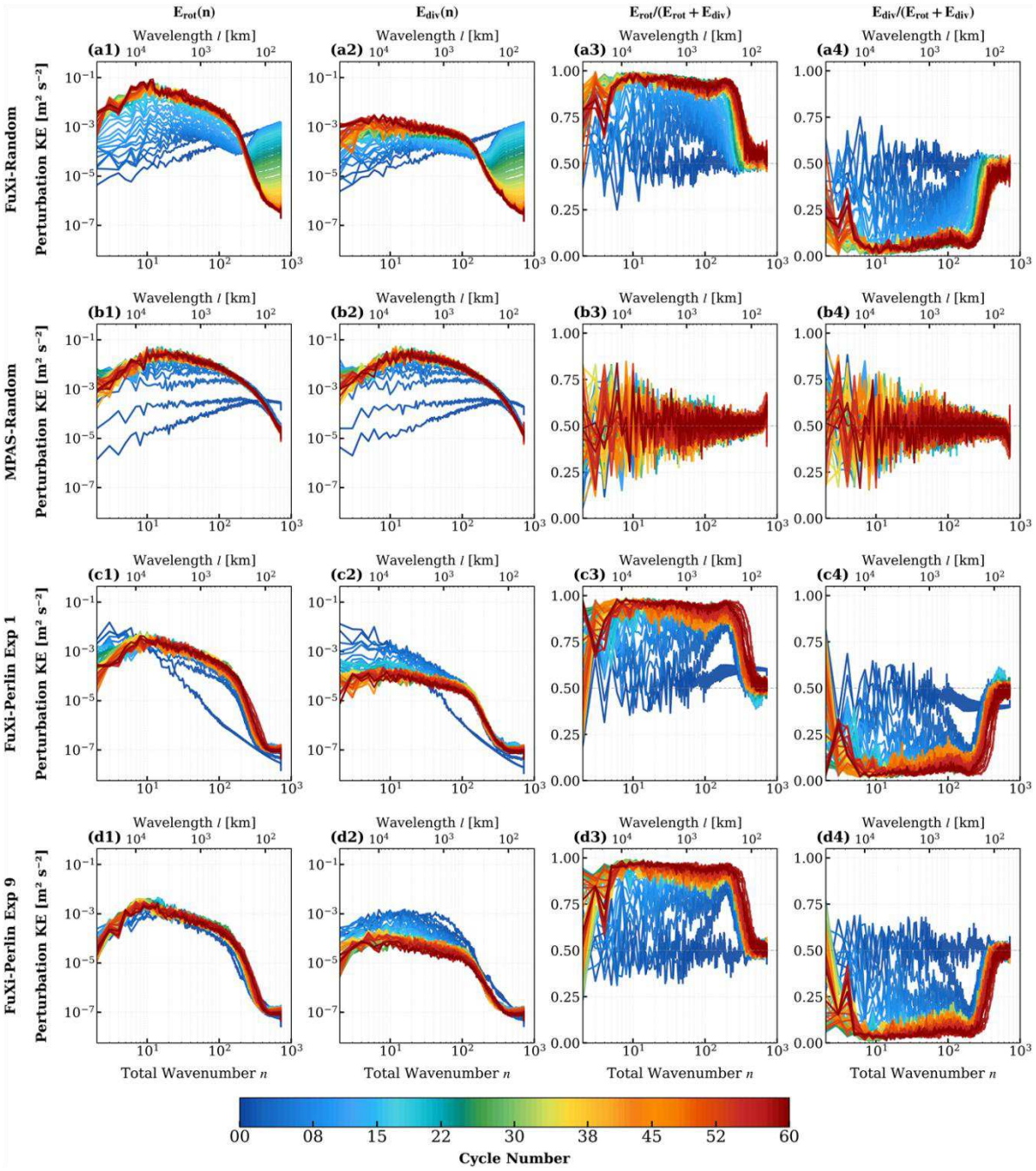
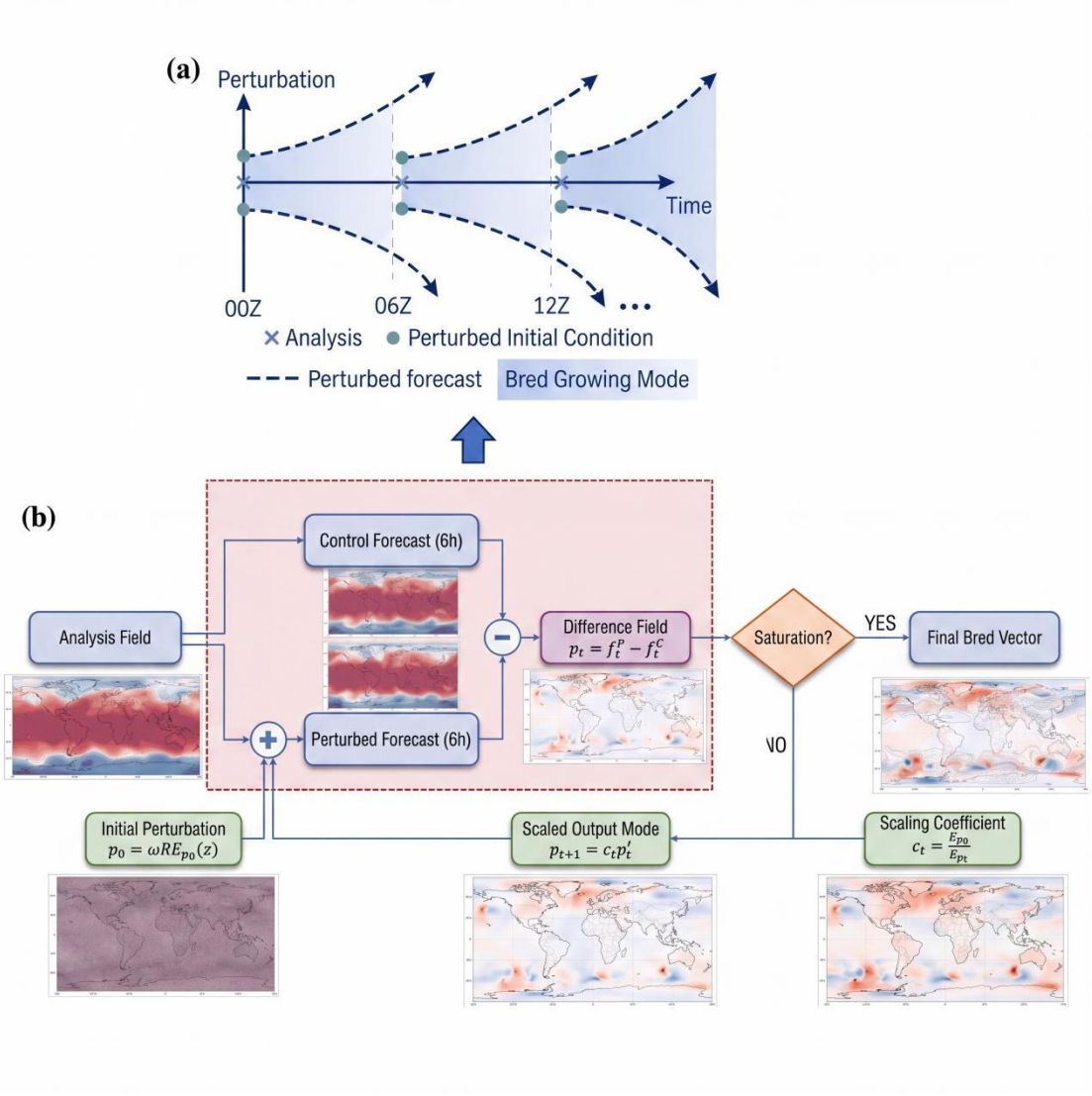



**Fig. 8 | Evolution of the rotational/divergent decomposition of the 500 hPa perturbation kinetic energy spectrum during the breeding cycle:** (**a**) FuXi random-number field, (**b**) MPAS random-number field, (**c**) FuXi Perlin noise Exp 1, (**d**) FuXi Perlin noise Exp 9. From left to right: rotational kinetic energy, divergent kinetic energy, rotational kinetic energy fraction, divergent kinetic energy fraction. Different colors represent different cycle numbers.




843

844 **Fig. 9 | Schematic diagram of the breeding cycle in the Breeding of Growing**
845 **Modes (BGM) method.** (a) Conceptual illustration of the BGM process. (b) Flow
846 chart of the breeding cycle with a 6-hour breeding period.

847

**Table. 1 Perlin noise parameters for the initial perturbation morphology sensitivity experiments.**

| Group | Experiment | Scale | Octaves | Persistence | Investigation Goal |
|---|---|---|---|---|---|
| Group 1 | Exp 1 | 2.0 | 4 | 0.5 | Spatial scale effect |
| | **Exp 2** | **5.0** | **4** | **0.5** | |
| | Exp 3 | 8.0 | 4 | 0.5 | |
| Group 2 | Exp 4 | 5.0 | 1 | 0.5 | Octaves effect |
| | **Exp 2** | **5.0** | **4** | **0.5** | |
| | Exp 6 | 5.0 | 8 | 0.5 | |
| Group 3 | Exp 7 | 5.0 | 4 | 0.1 | Persistence effect |
| | **Exp 2** | **5.0** | **4** | **0.5** | |
| | Exp 9 | 5.0 | 4 | 1.0 | |